

Plasma Erosion of Stressed Fused Silica and M26 Borosil

Aaron M. Schinder¹, Julian J. Rimoli², and Mitchell L.R. Walker³
Georgia Institute of Technology, Atlanta GA, 30324

The life of Hall effect thrusters (HETs) is limited by the erosion of the discharge channel wall. Erosion during long duration life testing of HETs produces surface features that are unexplained by present models. Anomalous erosion ridges are one such unexplained feature. An experiment is designed to test whether the evolution of surface features created by plasma-erosion is influenced by mechanical stress in the eroded material. Three pairs of fused silica samples and two pairs of M26 borosil are exposed to argon plasma at a vacuum facility operating pressure of 1.355×10^{-2} Pa. Ion current densities are ~ 3 mA/cm². A spring-loaded clamp compresses one sample of the pair to stresses ranging from 6 to 25 MPa. Equilibrium temperatures on the samples are modeled to be as high as 500 °C. Test fixture temperatures range from 225 to 288 °C during exposure. Detailed surface statistics are collected before and after each exposure with a Tencor P-15 contact profilometer. Optical and laser microscopy is conducted at set locations on the surface of each sample before and after exposure with an Olympus LEXT microscope. The results show that a 100- μ m pattern of parabolic depressions bounded by cusps develops on the fused silica samples. This cell pattern develops only in the presence of, and from, initial surface roughness (1.90 ± 0.54 μ m). The cell pattern can be explained as the result of the angle dependence of the sputtering yield of fused silica. The development of the final roughness pattern of the borosil samples is insensitive to initial surface roughness. The surface pattern on the borosil samples develops as a result of the heterogeneous microstructure of the material, and the difference in sputtering rate between BN grains and the silica matrix. No differences between the evolution of the stressed and control sample surfaces for loads of up to 24.99 ± 1.10 MPa (silica) and 24.1 ± 3.4 MPa (borosil) are detected after a 12-hr exposure.

Nomenclature

Ψ	=	amplification function (nondimensional)
\widehat{h}_0	=	initial Fourier transformed height profile (μ m/wave-mode)
\widehat{h}_t	=	final Fourier transformed height profile (μ m/wave-mode)
Y	=	sputtering yield (mm ³ /C or atoms/ion)
B_i	=	angle dependent polynomial coefficients (1/deg ⁱ)
E_{th}	=	sputtering threshold energy (eV)
E	=	ion impact energy (eV)

I. Introduction to HET Erosion

Hall effect thrusters (HETs) are a promising electric propulsion technology for applications such as station-keeping and primary propulsion. HETs typically operate at specific impulses of 1,300 – 3,000 s at efficiencies greater than 50%¹. HETs can be divided into stationary plasma thrusters (SPTs) and thruster with anode layer (TAL) types based on the insulating or conducting nature of their channel wall, respectively. SPT-type HETs, which use insulating ceramic channel walls, have seen the most development and use.

Multiple processes limit the useful operational lifetimes of HETs and hence the total impulse an engine can produce. HETs can fail suddenly due to cathode failure and thermal shock, but proper design and development can eliminate these as causes of thruster failure². However, the primary life-limiting mechanism for HETs, of the

¹ Graduate Fellow, Aerospace Engineering, 270 Ferst Drive, Atlanta, GA 30332-0150, AIAA Member.

² Goizueta Junior Faculty Professor, Aerospace Engineering, 270 Ferst Drive, Atlanta, GA 30332-0150, AIAA Senior member.

³ Associate Professor, Aerospace Engineering, 270 Ferst Drive, Atlanta, GA 30332-0150, Associate Fellow, AIAA.

traditional SPT type, is the plasma erosion of the discharge channel wall. Over the course of thousands of hours of operation, energetic ions sputter material from the annular discharge channel wall of a HET, wearing away the material in the 1-2 cm near the exit plane of the channel. When the channel wall is completely worn away in these areas, the magnetic circuit is exposed, and continued operation of the thruster will lead to the ejection of ferrous material into the spacecraft environment. Eventually, due to erosion of the magnetic material that generates the magnetic topology within the ionization and acceleration zones, the HET is unable to maintain efficient, stable operation. Because of the life limitations due to channel wall erosion, newer HET designs are being researched. These new HET designs, called magnetically shielded designs, use the shape of the magnetic field relative to the discharge chamber wall surface to deflect ions away from impacting the channel wall. These designs place much of the ion acceleration region, where ions attain sufficient energy to sputter material, downstream of the exit plane of the thruster³. However, magnetically-shielded HET designs are still in development, and older SPT thrusters designs used in contemporary spacecraft are still limited in operating life by channel wall erosion.

Before a HET is qualified to fly on a spacecraft, expensive and time-consuming qualification life testing is conducted to demonstrate the lifetime of all components of the thruster under a set of representative operating conditions. HETs must demonstrate an operational lifetime 1.5 times the lifetime required for the mission. These tests can involve more than a year of HET operating time and millions of dollars in consumables, facility operation, and labor. Qualification life testing is risky: before spending significant time on the test, it is unknown if the design will meet the mission requirements.

In order to make predictions about the results of thruster life testing, to reduce risk, and thruster operational life under untested conditions, computational models are used. Computational life modeling of a thruster makes predictions about the average erosion depth that will develop under certain operating conditions. The current state of the art uses 2D axisymmetric models of the plasma discharge to obtain potential contours and ion densities and velocities, which are then used as inputs to empirical sputtering yield models. The simulations model the evolution of the shape of the channel wall over time^{4,5,6}. Limitations to present erosion models are that they use only axisymmetric 2D models of the plasma and channel wall surface, and so are incapable of modeling the development of inherently 3D features. One such feature is the anomalous azimuthal ridges that have developed in the long duration life testing of many HETs. These ridges are 1-5 mm azimuthal ridges that develop in the eroded portion of the discharge channel. The BPT-4000⁷, SPT-100⁸, and PPS-1350G⁹ have developed these features during life testing. Figure 1 shows the anomalous erosion ridges on the BPT-4000. In addition to this, many parameters of these models, such as the electron mobility, or the sputtering threshold energy of the material are free parameters, adjusted to the empirical behavior of the thruster. Finally, in treating the material in the thruster as a homogenous isotropic solid with a sputtering yield depending only on the ion impact angle and ion energy, no basis for the formation of surface features exists in the absence of variations in the plasma.

The cause of the anomalous erosion ridges is still unexplained. Possible causes are variations in the plasma density and potential, variations in plasma sheath potential, or something arising from the plasma material interaction. One hypothetical mechanism that could explain the anomalous erosion ridges is that they result from an instability in the surface profile driven by the presence of variations in elastic strain energy. An average compressive load in the material produces a strain energy that is modified by the shape of the surface. Similar processes have been observed in acid etching of metals and stress corrosion cracking of materials¹⁰. In this study, the hypothesis that mechanical stress effects the development of surfaces during plasma erosion is investigated. In addition, detailed measurements of the evolution of material surfaces during plasma erosion are made. An experiment is designed to measure the development of surfaces on material samples placed under varying mechanical loads. Detailed surface profiles and microscopy are collected before and after the exposure of fused silica and M26 samples to argon plasma. The statistics derived from pre and post-test

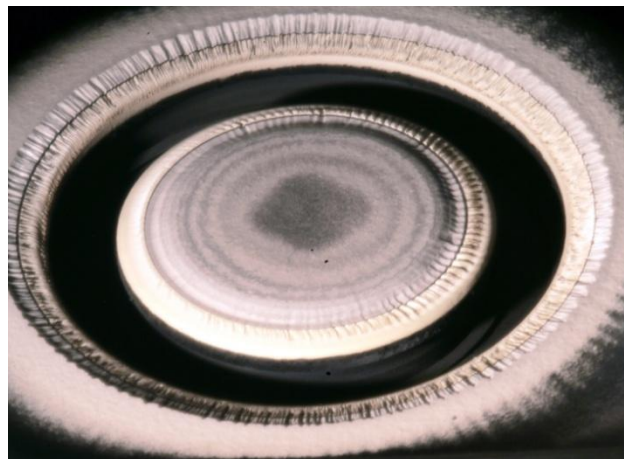


Figure 1. BPT-4000 after 10,400 hours of operation. Reprinted with permission from Aerojet Rocketdyne, from Ref 7.

line-scans reveal details about how the microscopic surface structures on amorphous and complex composite material develop.

In the next section, a brief overview of the design of the stressed erosion experiment is presented. Section III presents the results of the experiment. The microscopy of the pre and post-exposure surfaces is presented, along with surface profile statistics. Section IV discusses the results of the stressed erosion experiment, and presents mechanisms that explain the development of the surfaces on the fused silica and M26 samples.

II. Stressed Erosion Experiment

A. Chamber and Test Fixture

An experiment is designed to detect and characterize features amplified by a plasma erosion process. The experiment is specifically designed to detect any differences between the way a surface evolves during plasma erosion in the presence or absence of applied stress. It is designed to observe the combined effect, if any, of plasma exposure and applied stresses.

The source of the mechanical stress in an operating HET will be thermal loading from the plasma. Thermal modeling of HETs, described fully in Ref. 11, suggests that thermo-mechanical stresses as high as 6 MPa may be present in multi-kW class HETs with discharge channel walls composed of M26. The heat load on the interior of the channel wall leads to a temperature gradient across the wall, resulting in a compressive hoop stress on the inner faces of the channel. The flexural strength limit for M26 is around 34 MPa²⁰. Samples have been tested to destruction at 30-35 MPa. Stresses higher than the failure limit of the material will not be present in a properly designed HET. For this reason, the target range of stress for the experiment is between 6 and 30 MPa.

A test fixture is designed to apply uniaxial moment-free compression loads to material samples. This test fixture maintains the mechanical loads as the plasma heats the fixture by a series of conical disc-springs. Figure 2 shows the test fixture. A ball joint, and the motion of the spring-stack plunger ensures that compression applied to the sample is free of large bending moments. A cushion of PTFE tape on either end of the grips ensures that the mechanical boundary conditions at the grips are looser than built-in, and that the clamp transfers the load evenly from the grips. A spring-stack made of conical disc-springs, with an experimentally measured spring constant of 1597 ± 2 N/mm maintains the initial load to an amount quantified in characterization experiments and reported in Ref 11 and Table 2 as the system temperature increases during exposure to the plasma. The control sample is held one inch to one side of the loaded sample in a sheet-metal basket. The basket is attached to the side of the clamp in the y direction, into the page relative to Figure 2.

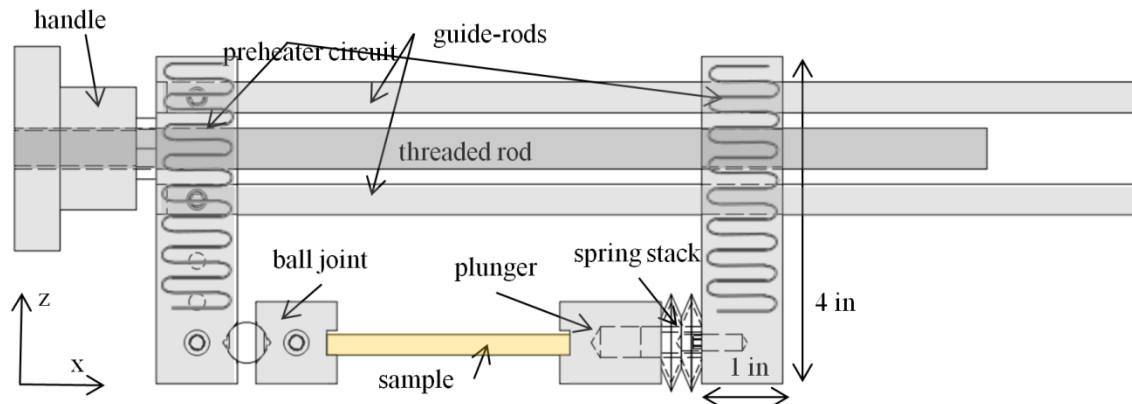


Figure 2. Experiment test fixture.

The samples and test fixture are positioned in the Georgia Tech Research Institute (GTRI) Ion Assisted Deposition (IAD) chamber. The IAD chamber is a Leybold APS 1104 chamber. The chamber has a diffuse plasma source capable of producing argon plasmas with ion energies of up to 110 eV at 120 V bias voltage. RPA measurements conducted with the plasma source operating at 140 V bias voltage show an ion energy distribution function (IEDF) centered at 130 eV with a standard deviation of 20 eV. The plasma source is operated at 120 V bias voltage for stable operation during exposure. The test fixture is positioned at a height of 32 cm from the chamber floor (7-8 cm from the top of the plasma source can) and centered over the plasma source. Figure 3 depicts the

positioning of the clamp over the source. Faraday probe characterization of the plasma source shows a 2/3 reduction in ion current density within a 4-cm radius of the source axis at a height of 40 cm above the chamber floor (15 cm above the plasma source can). Ion current densities are as high as 3 mA/cm² measured at 40 cm above the chamber floor along the axis of the plasma source. The IAD chamber base pressure is measured with a Leybold Ionivac at 2.3×10^{-4} Pa, with a pressure during 10 sccm Ar flow of $1.36 \pm 0.077 \times 10^{-2}$ Pa. The Ionivac is stated to have an accuracy of 15% in a pressure range from 10^{-6} Pa to 1 Pa. Further details of the plasma source and clamp characterization can be found in Ref 11.

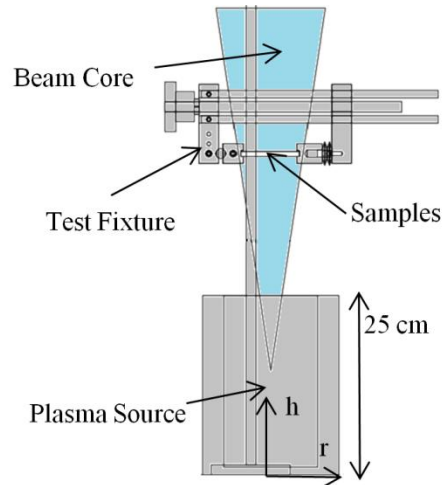


Figure 3. Diagram of test fixture in IAD chamber.

B. Sample Design and Material Selection

3x1x0.25 in. samples are used in the exposure experiment, so that the mechanical stress present in the material is close to a uniaxial load. The percentage of the stress along the axial direction is greater than 95% all stress components within the middle 50 mm of a 76.2 mm (3 in.) sample. In addition, the sample largely fits within the 8-cm beam core, and is short enough that the clamp can extend to accommodate the sample within the confines of the chamber. The maximum wavelength resolvable in a Fourier transform of the surface line-scan is a function of the length of the scanned region. Having a long sample is desirable to capture surface profile information at long wavelengths.

Two materials are selected for the experiment: Fused silica and M26 borosil composite. Fused silica is chosen because it is an amorphous, isotropic solid. This is desirable so that effects due to the presence of mechanical stress or due to the initial surface are distinguishable from effects arising from the material microstructure. Fused silica samples are procured from Technical Glass Products. Boron nitride/silica composites, similar in composition to M26, are of interest because they are commonly used for HET channel walls^{4,12,13}. M26 is a composite material (60% BN, 40% silica by mass) with a complex heterogeneous microstructure. M26 is formed by hot-pressing boron nitride (BN) and silica powder. M26 is a much more complex material than fused silica or purer grades of boron nitride (BN). Figure 4 shows a SEM image of a representative cross section of M26 and shows that the material is composed of triangular flakes of BN, 10's of μm wide by 100's of nm thick interspersed in a silica matrix. Rectangular M26 samples are acquired from St. Gobain, and machined into 3x1x0.25 inch samples to fit within the testing region and test fixture.

In order to use a strain measurement to derive the applied load and stress within a material, the elastic moduli of the material must be known. Measurements of the elastic moduli of the two materials are conducted with 1x1x0.25 in. samples instrumented with WK-02-062AP/W strain gages, and an Instron 5900 material testing device. Three to five load ramps of up to 1000 lb_f are conducted on samples placed in a compressive frame. These tests yield experimental values for the elastic moduli of the materials. For fused silica, a value of 58.7 ± 2.4 GPa was obtained. For M26, a value of 22.8 ± 3.1 GPa was obtained. The elastic moduli allow the conversion of the strain measured by attached strain gages into stress in the material.

In order to measure the stress applied to the samples in the IAD chamber, the samples are instrumented with strain gages. The 3x1x0.25 in. test samples are instrumented with WK-02-062AP/W strain gages from Vishay Micro Measurements. These strain gages have a resistance of 350 Ω , a gage factor of 2.01, and the measured strain signal

wanders less than 5 microstrain over the course of 5 minutes. The strain gages are used, along with the measurements of the material Young's modulus, to measure the initial room temperature load applied to the samples in the test chamber. Samples are prepared by pre-roughening the surface with a sequence of silicon-carbide grit. The samples are roughened with 320- then 500 -grit SiC using a cover glass, until a uniform random surface finish is attained, then the surfaces are cleaned thoroughly with an alcohol bath, cotton-balls, and an air-blast.

C. Test Procedure

The experiment is conducted in three phases: A pre-exposure phase, an exposure phase, and a post-exposure phase. In the pre-exposure phase, each of the samples is prepared and instrumented with a strain gage. Following that, each of the samples is imaged with the Olympus LEXT 3D confocal microscope in several pre-planned locations. The LEXT produces both computer-enhanced, focus-adjusted optical images and 2D laser surface height profiles. The surface height profiles show the topographical height variations of the surface as a function of position on the surface. The location of each image is measured using the microscope motion stage from the lower left corner of the sample, so that the same location can be imaged post-test.

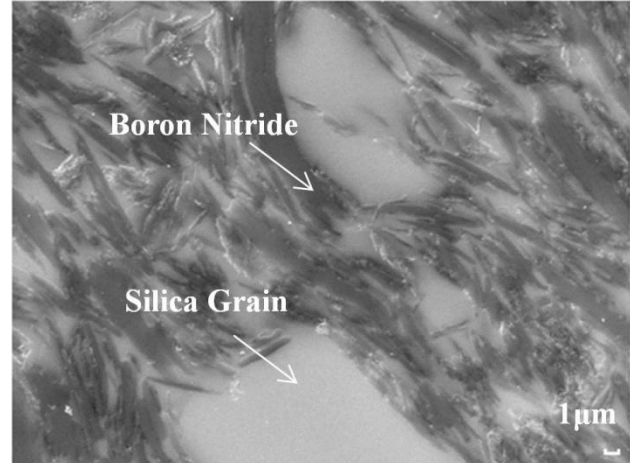


Figure 4. SEM of M26 borosil cross-section.

A series of line-scans of each sample surface is taken with the Tencor P-15 contact profilometer. Each scan in the series is 50 mm along the long-axis of the sample surfaces. Each scan is displaced along the short axis of the sample by 20 μm. The Tencor P-15 profilometer has a vertical resolution accurate to within 0.5 Å, and a vertical range of 327 μm. In practice, a variability of ± 0.05 μm on optically smooth fused silica is observed.

During the exposure phase, a pair of samples is placed in the test fixture. The loaded or experiment sample is placed in the grips of the test-fixture clamp. The unloaded control sample is placed in a 304 stainless steel basket positioned to the side of the test-fixture. The sample strain gages are wired to the strain gage data acquisition system. A thermocouple is placed on the test fixture to provide a measurement of the average test-fixture temperature. The test fixture temperature is measured to provide a calculation of the thermal expansion of the test-fixture screw, and the relaxation of the room-temperature load. The approximate temperature of the sample is calculated based on thermal modeling of the clamp-sample system. Additional testing was also conducted with a thermocouple mounted on the rear surface of the sample during a short plasma exposure. The test fixture is positioned over the plasma source. After loading the experiment sample to the desired load, using the strain gage to measure the applied load, the chamber is evacuated. The samples are exposed to argon plasma, 3 mA/cm², 100 eV, for 12 hours. Post-exposure, the samples are removed from the chamber.

During the post-exposure phase, the pre-test surface measurements are repeated. Images are taken of the regions of interest on each sample with the Olympus LEXT. Post-exposure line-scan profiles are taken with the Tencor P-15 contact profilometer. Of particular interest are statistics derived from the Fourier transformed line-scan height profiles. An "amplification function", denoted Ψ , can be derived from pre-test and post-test line-scans. This function of spatial frequency contains information about which spatial-frequency (or wavelength) features on the surface are being amplified by the erosion process, and which are being damped. If features similar to the erosion ridges are forming, Ψ should be greater than zero in the region corresponding to the ridge wavelength (1 - 5 #/mm). Ψ is calculated by equation 1. In equation 1, \widehat{h}_t is the pre-test Fourier transform of a line-scan, \widehat{h}_0 is the post-test Fourier transform of a line-scan, ω is the spatial frequency (rad/m), and Ψ is a nondimensional function showing which waves are growing ($\Psi > 0$) and which are being damped ($\Psi < 0$). Fifty line-scans are taken pre and post-test, and their Fourier amplitudes are averaged to reduce variability in the data.

$$\Psi = \log_{10} \left(\frac{|\widehat{h}_t(\omega)|}{|\widehat{h}_0(\omega)|} \right) \quad (1)$$

This section provides a brief overview of the stressed erosion experiment, and its procedures. More details about the design and validation of the experiment can be found in Ref. 11.

III. Results

A. Fused Silica Exposure Results

Four exposures with fused silica samples are conducted. One exposure is conducted with smooth (as manufactured) samples, with surface variations less than $\pm 0.05 \mu\text{m}$ as measured by the Tencor. The purpose of the smooth samples is to test the importance of initial surface roughness to the resulting final patterns that develop. Initial rms roughnesses on the fused silica samples are $1.90 \pm 0.54 \mu\text{m}$. Three of the exposures use pre-roughened samples, with a series of increasing loads applied to the loaded sample. **Error! Reference source not found.** shows a summary of the fused silica exposures. The loaded and control sample numbers are given so that data may be compared with the conditions of each exposure. The equilibrium temperature is the fixture temperature for the majority of the exposure (after approximately 30 minutes of warm-up time in the plasma beam) takes place, measured by the type-K thermocouple on the fixture. The relaxed stress state is the stress in the sample, calculated by the relaxation characterization model, for the given equilibrium temperature and initial strain. The duration of each exposure, and the z-position of the fixture above the chamber floor (altitude in the table below) is given.

Samples are numbered with a unique identifier that all test data is indexed to. Sample series SA is composed of $3 \times 1 \times 0.25$ in. samples fabricated from fused silica. Sample series SC is composed of $3 \times 1 \times 0.25$ samples fabricated from M26. Other sample series (S, SB, SD) refer to other sample sizes and materials used for other tests, such as destructive testing and Instron testing. Sample SA2 and SA3 were expended in an exposure under different plasma conditions.

Table 1. Exposure overview for fused silica exposures.

Exposure	Exp. 1	Exp. 2	Exp. 3	Exp. 4
Loaded Sample	SA7	SA1	SA8	SA6
Control Sample	SA4	SA5	SA9	SA10
Initial Stress State (MPa)	9.6	17.5	18.1	29.1
Equilibrium Temp ($^{\circ}\text{C}$)	288 ± 12	225 ± 8	224 ± 5	243 ± 5
Relaxed Stress State (MPa)	6.00 ± 1.01	14.36 ± 1.01	14.94 ± 0.97	24.99 ± 1.10
Relaxed Stress State (% orig)	62.5 ± 10.5	82.05 ± 5.79	82.57 ± 5.36	85.87 ± 3.79
Duration (hrs)	11	11	11	11
Pre-Roughened	Yes	Yes	No	Yes
Altitude (cm)	31	32	32	32

*Three out of five $1 \times 1 \times 0.25$ in -samples cracked at a load over 30 MPa, so the initial sample loads all fall under 30 MPa.

Roughness statistics were derived from the pre-test and post-test amplification functions. Post exposure rms roughnesses of $2.20 \pm 0.57 \mu\text{m}$ are present on the fused silica samples. Statistics for 50 line-scans are averaged from the pre and post-test surfaces. Figure 5 shows 7-point spatial frequency averages of these statistics for spatial frequencies up to 80/mm. Sample SA4 (control sample) has different roughness statistics than the other samples tested due to being prepared with a different sequence (240, then 320 grit) of SiC powder. The ratio between the pre-test and post-test surface statistics (which, in the logarithmic scale of Figure 5, appears as a difference between pre and post-test statistics) is the same for both samples. This demonstrates that a growth process is operating on the initial surface structure of the samples to produce the final surface structure. The post-test roughness statistics are proportional to the pre-test statistics.

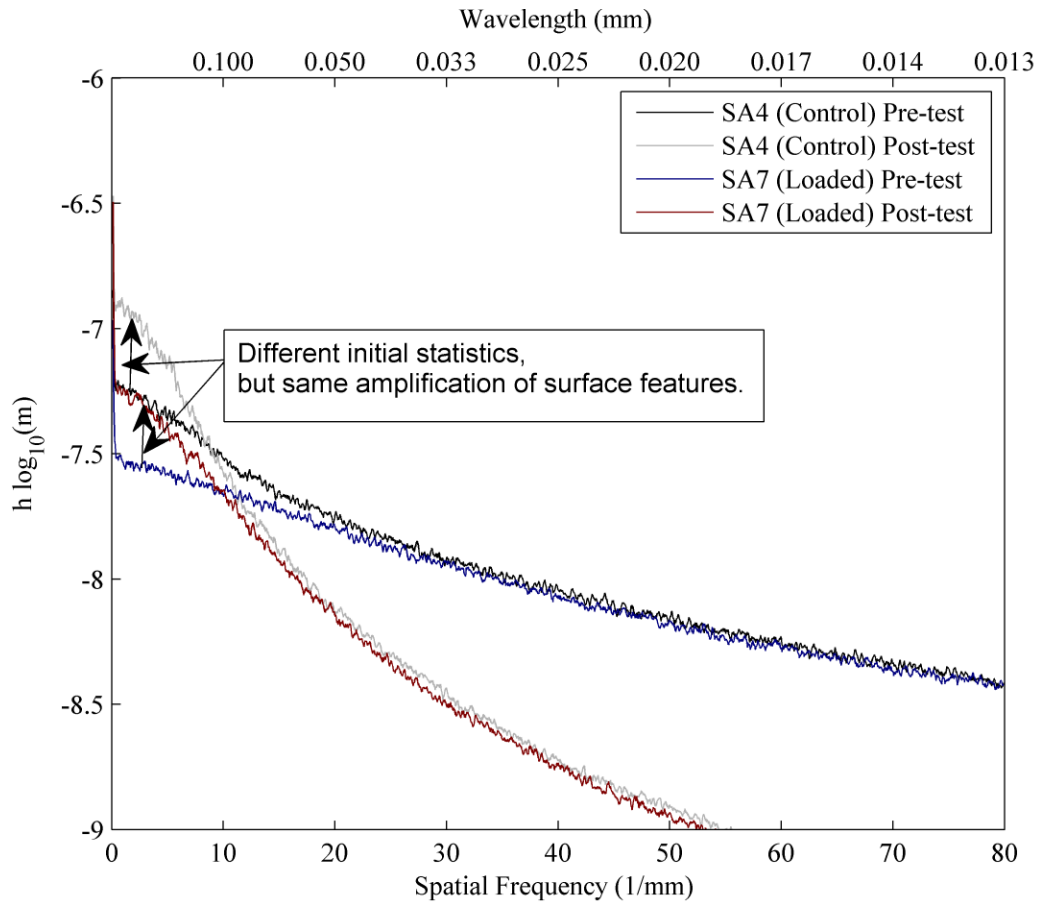


Figure 5. Pre versus post-test averaged Fourier transformed amplitude as a function of spatial frequency for exposure 1, fused silica.

Figure 6 shows an overlay of the amplification functions derived from these line-scan statistics. The uncertainty or variability in the measurement of Ψ is ± 0.15 or so, therefore 7-point spatial frequency averaging reduces the noise so that the series are more clearly distinguishable. Each loaded sample and control sample amplification function lie on top of each other to within ± 0.05 , and cannot be distinguished to within even the variability of the spatial-frequency averaged data. No difference between how the loaded and control sample's surfaces change between pre and post-test is apparent. Variations of about ± 0.1 are seen for Ψ between each exposure pair.

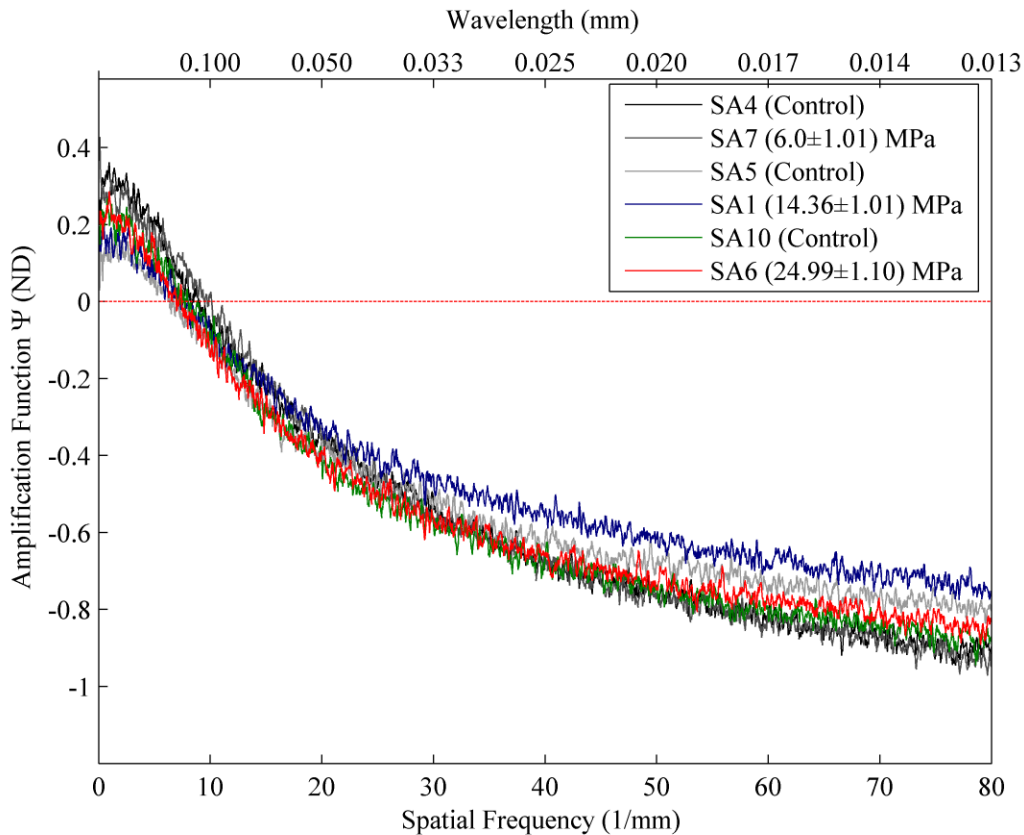


Figure 6. Amplification function (with 7-point spatial frequency average) as a function of spatial frequency.

Figure shows ratio of pre vs. post-test amplitude. $\Psi > 0$ shows spatial frequencies that are growing.

Figure 7 shows laser height-maps and laser images of the center locations of two fused silica surfaces, taken before and after the exposure to the plasma. Pre-exposure, each surface is an isotropic random white-noise pattern. After exposure, a pattern of cells covers the surface of the pre-roughened samples. This cell pattern is composed of smooth parabolic depressions bounded by sharp-edged cusps. The surface has the overall appearance of a plane divided into Voronoi-like cells. Each cell is a cup (concave) not a bubble (convex).

For exposure 3, two samples, SA8 (loaded) and SA9 (control) are exposed to the same load conditions as exposure 2 (14.9 MPa). The surfaces of these samples are not pre-roughened, and are left optically smooth ($\pm 0.05 \mu\text{m}$), except for a small area of SA9 (control). This area is scored with the tip of a 1/16 in. fine-pointed screwdriver to create a limited region where initial surface roughness is present. Figure 8 shows the comparison of the scored region before and after exposure. Post-exposure, the unmarked regions of the smooth samples remain smooth in the microscope images taken with the LEXT. No apparent surface features resulting from a growth process appear to be present, as expected, because there are no surface features to grow from. However, the marked region shows the beginning of the same cell structure seen on the pre-roughened samples.

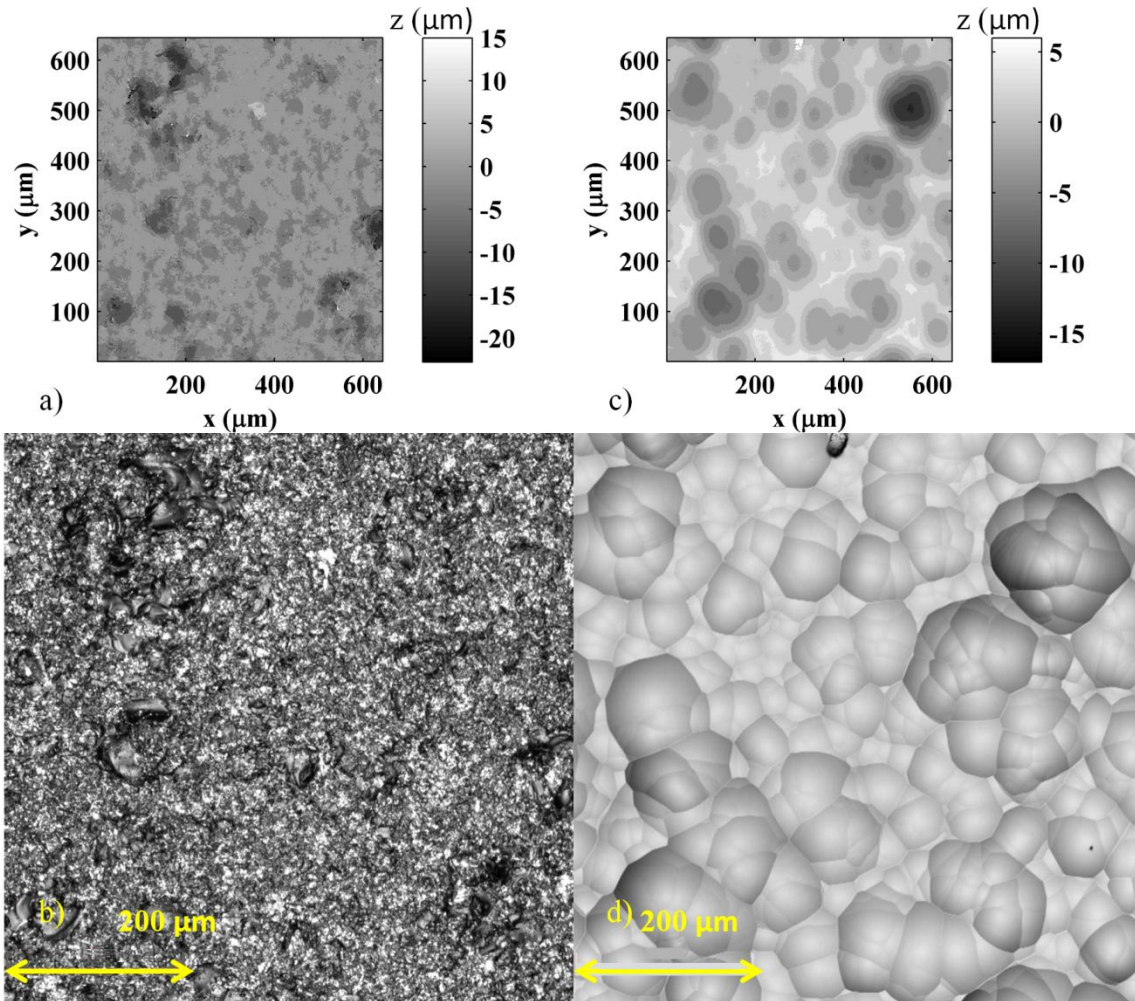


Figure 7. Pre and post-test sample microscopy: SA6 (loaded), 20x, center of exposed surface, a, b) pretest height and laser image, c, d) post-test height and laser image.

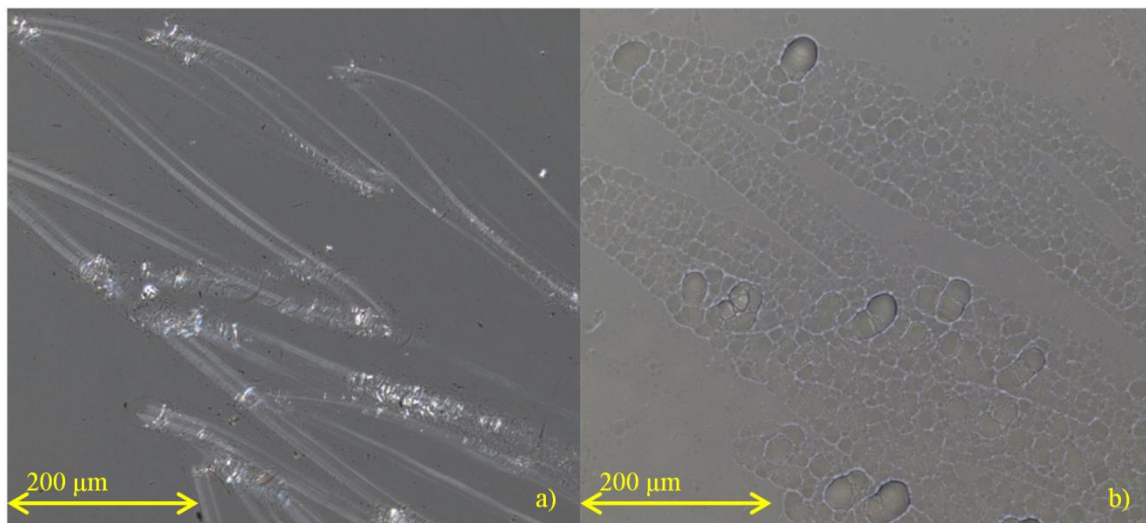


Figure 8. SA9 (control) laser microscopy, scored region, a) pre- and b) post-exposure.

B. M26 Borosil Exposure Results

In addition to the fused silica exposure, M26 is also loaded and exposed in the IAD chamber. Four 3x1x0.25 in. M26 samples are exposed in two exposures. Each sample is machined, and then the surface was prepared with SiC polishing grit, as with the fused silica samples. A pre-test surface roughness of $1.55 \pm 0.10 \mu\text{m}$ is present due to the polishing. The surfaces of each sample are cleaned with an alcohol bath, water, and air blasting until an even surface finish is present.

Table 2 presents the conditions for each exposure, and the calculated relaxed loads given the equilibrium test temperatures. Prior to exposing the M26 samples to the plasma, one of the 3x1x0.25 in. M26 samples is tested to destruction in the clamp. The M26 sample fails at a strain of 1350 microstrain, or a stress of $30.8 \pm 4.2 \text{ MPa}$. Initial test loads are chosen to fall under this threshold to avoid prematurely cracking the samples. After each exposure, average erosion depths of $12.5 \pm 2.5 \mu\text{m}$ are developed on each sample surface.

Table 2. M26 borosil exposure conditions.

Exposure	Exp. 1C	Exp. 2C
Loaded Sample	SC1	SC4
Control Sample	SC3	SC5
Initial Stress State (MPa)	23.4 ± 3.1	27.2 ± 3.7
Equilibrium Temp ($^{\circ}\text{C}$)	241.3 ± 15.6	258.6 ± 2.4
Relaxed Stress State (MPa)	20.6 ± 3.3	24.1 ± 3.4
Relaxed Stress State (% original)	77.6 ± 12.3	77.8 ± 1.1
Duration (hrs)	12	12
Pre-Roughened	Yes	Yes
Altitude (cm)	32	32

*SC2 was tested to destruction in the clamp.

Figure 9 shows an overlay of the pre and post-test roughness statistics measured on the exposed surfaces of the M26 samples. Unlike the fused silica roughness statistics, it is not the difference between the pre and post-test statistics that is similar between samples, but the post-test statistics. This similarity in post-test statistics indicates that the post-test surfaces that develop on the M26 samples are insensitive to the pre-test surfaces that are present. The post-test surfaces are sensitive to pre-test statistics with fused silica. Unlike fused silica, M26 has a complex heterogeneous microstructure, and the difference in the sputtering yield of the components present in the material volume is the dominant influence on how the surface evolves. In the fused silica samples, due to the simple amorphous microstructure, the only input to the evolution of each surface is the pre-existing surface structure. As with the fused silica, no apparent differences are present in the pre and post-test surface statistics between loaded and control samples. Each post-test Fourier transformed roughness curve is the same to within $0.01 \mu\text{m}/\text{wavemode}$.

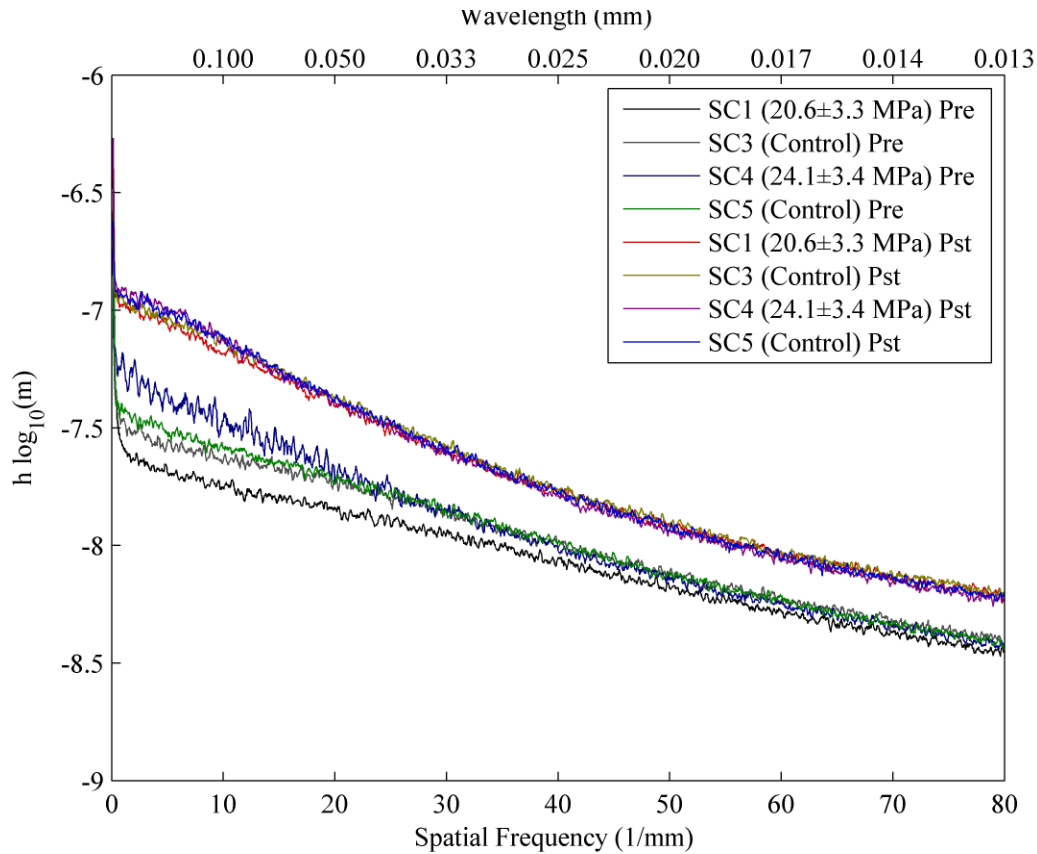


Figure 9. Pre vs. post-exposure averaged Fourier transformed surface amplitude as a function of spatial frequency (surface roughness statistics) for M26.

Figure 10 shows visible light and laser surface height profile images of the center of sample SC3. Pre-test, the surfaces are whitish in color, without visible differentiation between silica and BN grains. Post-test, all surfaces have evolved into shapes defined by the nature of the underlying grains. M26 is a composite of BN flakes in a silica matrix. In the post-test images shown, flat flake-like regions (the BN flakes) protrude at random angles from a background of silica. Regions composed of exposed silica erode slightly faster to form depressions. The nature of the surface appears to be determined almost entirely by the atomic-sputtering properties of the grains. All samples have surfaces with similar appearances. The RMS roughness is greater post-exposure: $4.26 \pm 0.66 \mu\text{m}$. In the post-exposure visible light images, the BN flake/protrusion regions appear darker in color.

Higher magnification images taken with the Olympus LEXT have a finer vertical resolution, and show the BN ridge phenomenon more clearly. Figure 11 shows a high-magnification image of a BN-rich region in the dark lower-left corner, protruding from the surrounding material. In the lower left corner of Figure 11, a dark BN rich region protrudes from the surface. Additional smaller BN-rich regions in the upper left also produce elevated features.

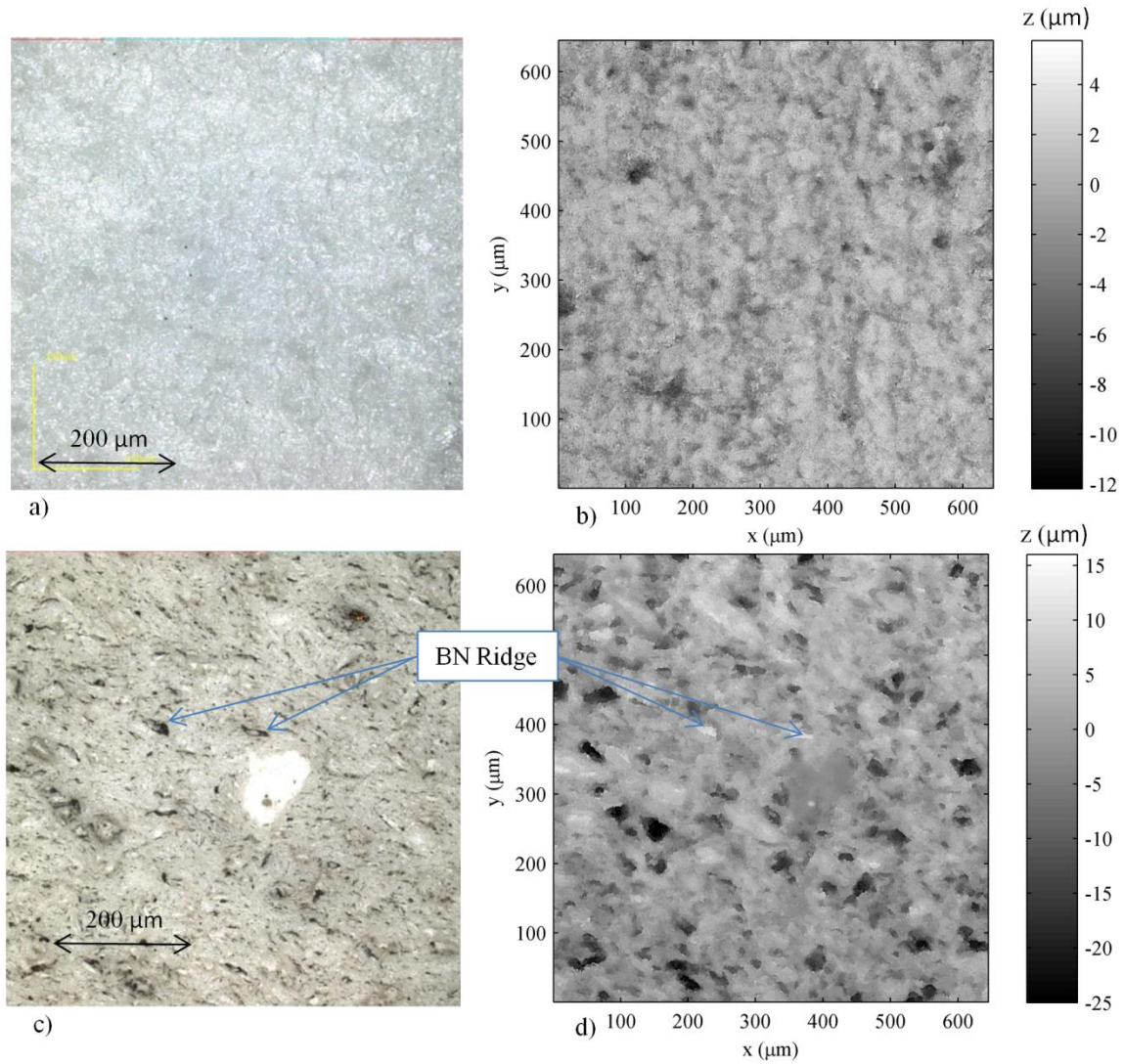


Figure 10. SC3 (control), 20x, Pre-exposure surface a) visual image, b) surface height profile, Post-test surface c) visual image, and d) surface height profile.

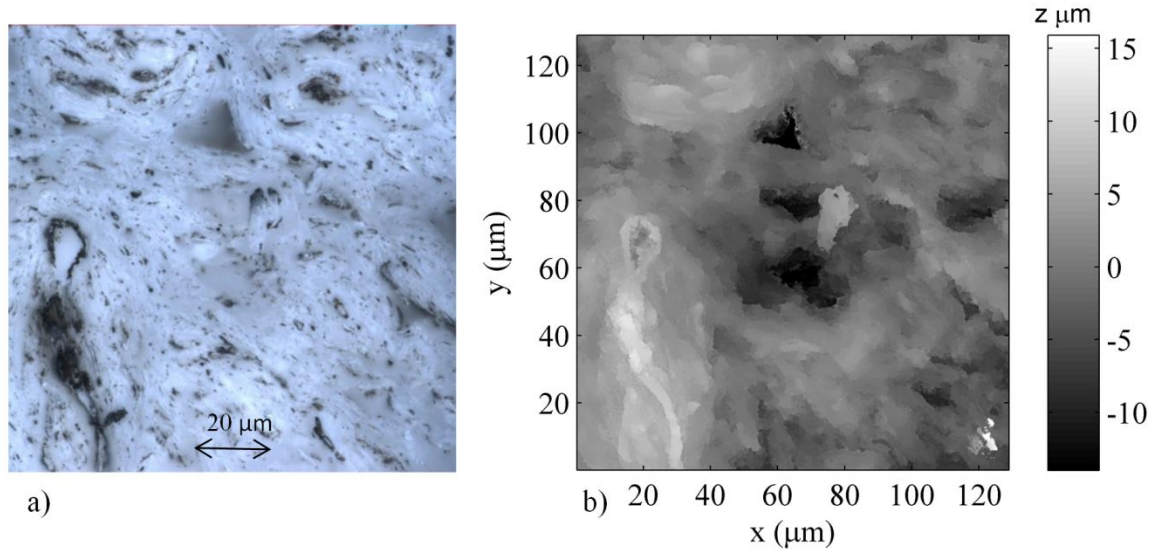


Figure 11. SC1 (loaded) 100x magnification post-exposure a) visible light image, b) laser surface height map.

IV. Discussion

The results from the stressed erosion experiment show two different primary mechanisms for the surface evolution of each material. For fused silica, the final surface profile is shown to be a function only of the initial surface profile. Surface roughness statistics are proportional to initial surface roughness statistics in a highly consistent way across all exposed samples. For M26, the final statistics are insensitive to the initial surface roughness statistics. All samples attain the same final surface roughness statistics to within $0.01 \mu\text{m}/\text{wavemode}$ at the same erosion depth. As stated in the last section, the main difference between the fused silica samples and the M26 samples is the absence (in the case of fused silica) or presence (in the case of the composite microstructure of M26) of microstructural detail in the material. In the next two sections, hypotheses and models that explain the evolution of each material are given. The final section discusses how the gas used, and surface temperature effect the experiment. For stresses of up to 25 MPa, no difference between the evolution of the loaded samples and control samples has been observed. No evidence has been for the dependence of plasma erosion on mechanical stress in fused silica or M26.

A. Development of Surfaces under Angle-Dependent Sputtering Yield

A simple hypothesis to explain the growth of the cell patterns in the exposed fused silica surfaces is that these patterns result from the angle dependence of the sputtering yield of the material. Under normal ion bombardment, the local angle that the surface makes to the incoming ions modifies the local sputtering yield, and speed of erosion. In sputtering yield theory and experiment, the yield tends to peak at ion incidences of 50° to 80° from the surface normal of the target. In a semi-infinite medium, there will be an angle at which the repulsive action of the surface atoms prevents the ions from penetrating into the target (and hence a reduction in yield from the maximum). At lower angles, the size of the region of energized target atoms that lie close enough to the surface to allow atoms to escape the target scales as $1/\cos(\theta)$, with θ being the ion angle relative to the surface normal. If the ion mass is greater than the atomic mass of the target material, as is the case for argon and xenon with a SiO_2 target, then $1/\cos(\theta)$ is a good model. If the masses are more nearly equal, the angle dependence scales as $1/\cos(\theta)^{5.3}$ ^{14,15}.

For the following analysis, a curve fit of the modified Yamamura form is made to empirical angle dependent yield data collected by Yalin *et al.* for xenon sputtering of fused quartz¹⁶. The form of the model is given in equation 2, and the coefficients to the model are given in Table 3. The angle dependence of the yield is shown in Figure 12, showing that a 3rd-degree polynomial fit to the data peaks at 55° ion incidence to the surface normal.

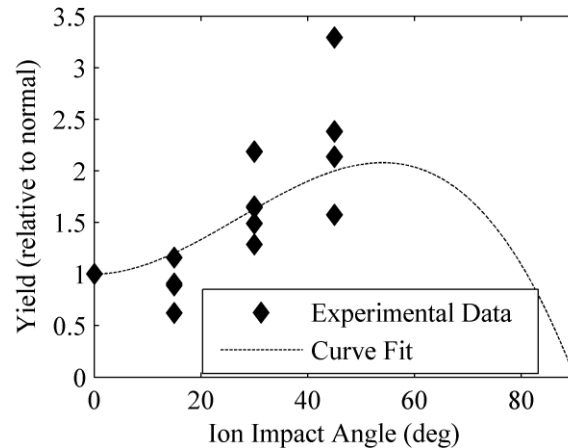
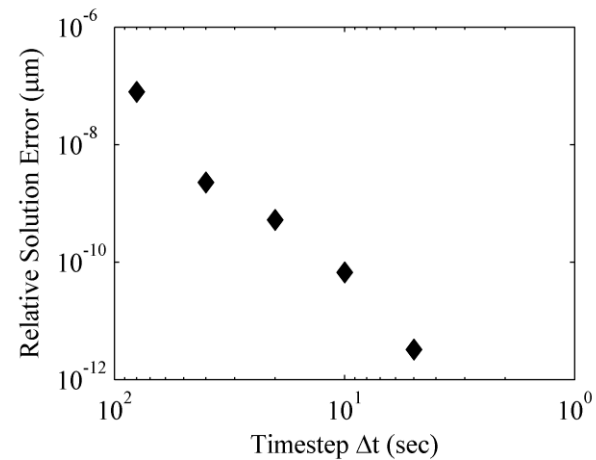
$$Y(E, \theta) = f(\theta)g(E) = (B_0 + B_1\theta + B_2\theta^2 + B_3\theta^3)k\sqrt{E} \left(1 - \sqrt{\frac{E_{th}}{E}}\right)^{2.5} \quad (2)$$

Table 3. Yield model fitting coefficients.

Variable	Value	Unit
k	5.0×10^{-3}	$\text{mm}^3/\text{C-eV}^{0.5}$
E_{th}	15.0	eV
B_0	1	1
B_1	0	1/deg
B_2	1.11×10^{-3}	1/deg ²
B_3	-1.37×10^{-5}	1/deg ³

Townsend noted that due to the higher sputtering yield of surfaces at an angle to an ion beam, certain initial surface profiles, such as spheres or sinusoidal surfaces would develop, over time, into cones or cusps as erosion proceeds¹⁵. A one-dimensional simulation of the evolution of a surface profile by atomic sputtering is constructed which demonstrates this behavior. The simulation calculates the rate of erosion at each point along a surface profile as a function of the surface normal of the neighboring area elements. The simulation evolves the surface profile in time, producing eroded surface profiles from uneroded surface profiles. Timesteps of 5 s are used to simulate the evolution of surface profiles with a 0.4 nm horizontal spacing between nodes. The model uses ion current densities of 10 mA/cm² and ion energies of 100 eV, similar to conditions in the IAD chamber experiment. Figure 13 shows relative error as a function of timestep. This demonstrates that the simulation is well converged for 5-s timesteps. The reference solution is one run at 2.5-s timesteps, to which the other solutions are compared.

A 500- μm section is taken from the pre and post-test line-scans for sample SA6 (loaded). A simulation of the erosion of the top surface is propagated forward in time. At erosion depths similar to the ones reached during the 11-hour experimental exposure, a profile with features similar to the experimental post-test surface is observed. Figure 14 shows the pre and post-test line-scans in blue and several time-steps of the simulated evolution of the top profile in black. The actual surface is two-dimensional, and so there is an extra dimension for the profile to be off-normal to the ion beam. However, even with a one-dimensional simulation, features of a similar depth and profile to the post-test surface develop.

**Figure 12. Sputtering yield of fused quartz as a function of ion incidence angle. Data from Ref 16.****Figure 13. Convergence: Error relative to 2.5-s timestep solution as a function of timestep.**

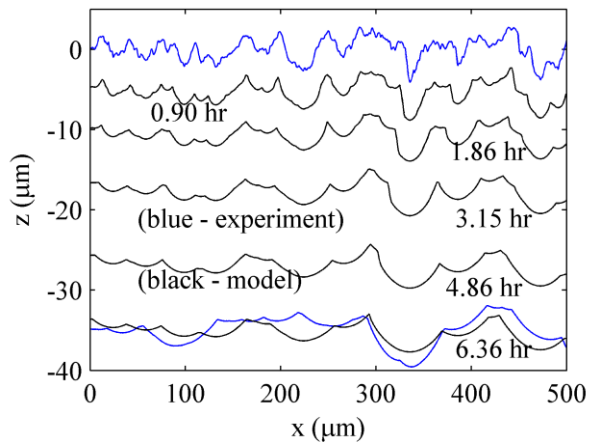


Figure 14. Measured and simulated surface profiles as a function of time.

Fifty 1-mm long subsets are taken from the 50-mm long line-scans recorded by the Tencor. The pre-exposure line-scans are propagated using the model to the average erosion depth attained during exposure. From the simulated post-exposure line-scans, Fourier statistics similar to the experimental statistics in Figure 6 are derived. Figure 15 shows a comparison of the amplification function for the experimental and modified profiles for sample SA6 (loaded). These amplification functions have less spatial frequency resolution than the ones shown in Figure 6 due to the smaller length of the simulated domain, but show the same general trend. Both the simulated and experimental amplification profile show growth of features with a longer wavelength than 0.1 mm, and damping of smaller wavelengths. The amplification statistics agree well until approximately 30 mm^{-1} . The simulation shows less damping at higher spatial frequencies than the physical process. This might point to the existence of a smaller order diffusive process not captured in the model. Arguably, high spatial frequency information, due to the smaller order of magnitude initial and final amplitudes, is noisier and less important to defining the pre and post-test surfaces. The agreement at spatial frequencies below 30 mm^{-1} corresponds to the qualitative similarity between the modeled and experimental post-test surfaces.

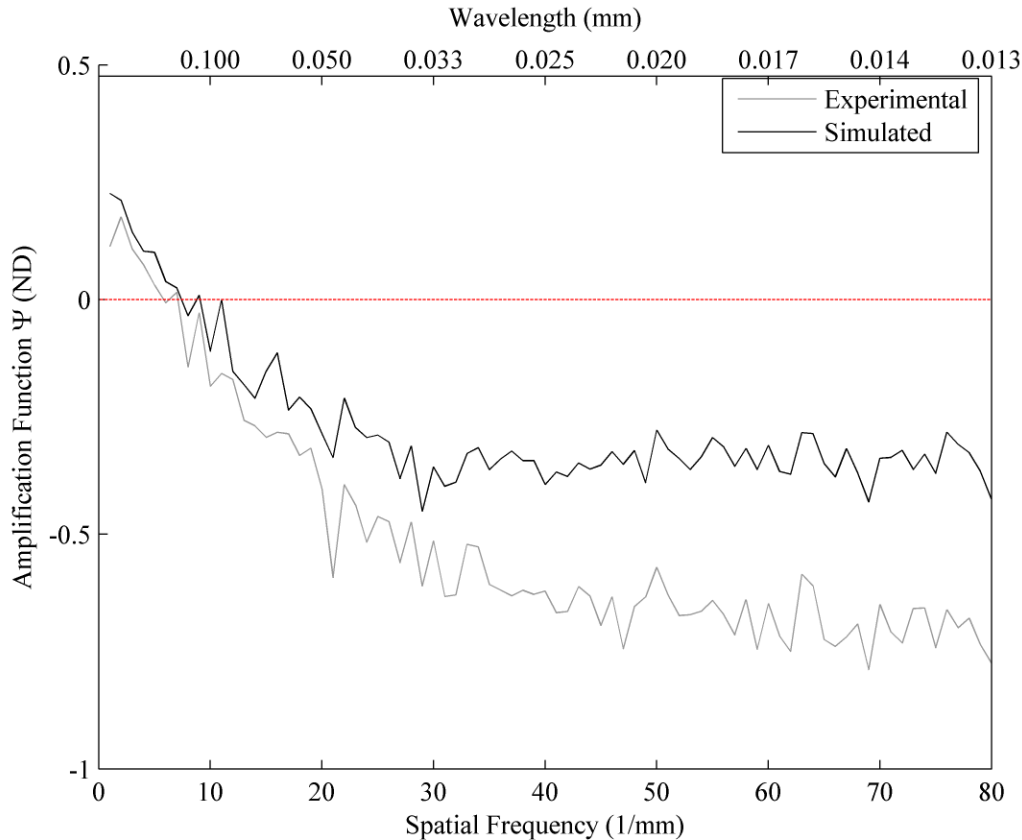


Figure 15. Amplification function Ψ as a function of spatial frequency for experimental and simulated profiles.

B. Evolution of Surface Features in Heterogeneous Materials under Plasma Erosion

The surface features generated in the more complex borosil composite are best explained as resulting from the differences in sputtering yield between the boron nitride and silica components of the composite. Boron nitride has a lower sputtering yield in general than silica when bombarded by plasma. Ref 17 provides details of a 3D model of the erosion of M26 borosil. In this model, independent sputtering yield models are used for exposed boron nitride and exposed silica to model the evolution of a 3D surface profile as the plasma erodes material in a simulated domain.

In the paper, the model is used to successfully reproduce some surface features that are observed in SEM microscopy of the eroded channel wall of the AFRL/UM P5. The AFRL/UM P5 is a 5-kW HET tested for several thousand hours at the University of Michigan¹⁸. Figure 16 shows incoming ions at an angle to a complex surface structure impacting a surface composed of low-yield BN and high-yield silica. At an angle to the surface, a cliff-and-valley structure is produced as the BN shields the higher yield fused silica material from incoming ions. Figure 17 shows the surface profiles produced by the model in comparison with the cliff and valley structures resulting from the long-term operation of the AFRL/UM P5.

The stressed erosion experiment exposed the M26 samples to a normally incident ion beam. In this case, the shadowing effect is less important, but the long thin BN grains still protrude from the surface, creating surface profiles that have been observed in this experiment. Even if the initial surface were completely flat, surface features of a certain character and equilibrium roughness would eventually develop from erosion into the material due to the material microstructure.

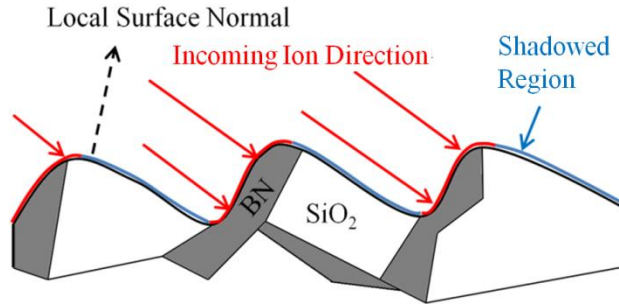


Figure 16. Ray-tracing approach to modeling differential sputtering.

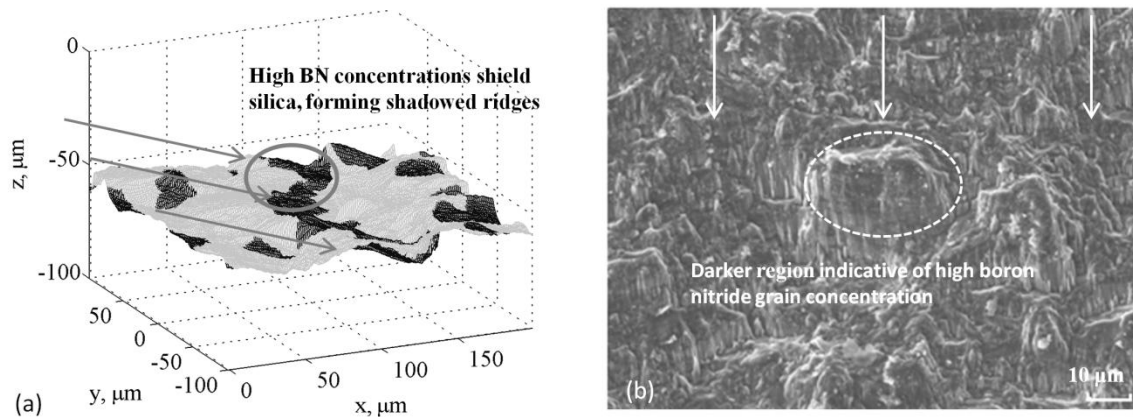


Figure 17. a) Simulated erosion surface, b) SEM image of highly eroded section of channel wall.

C. Effects of Ion Mass and Temperature

In the stressed erosion experiment, the equilibrium temperature that the clamp and samples attain is important primarily in how much relaxation is produced due to the thermal expansion of the clamp screw. Prior research on atomic sputtering by Sigmund¹⁴ and Rosenberg and Wehner¹⁹, states that the sputtering yield of a target material is insensitive to the material temperature. The stressed erosion experiment uses argon gas instead of xenon, which is commonly used in HETs. However, the sputtering yield for the energies of interest in HET physics (10^2 's- 10^3 's of eV) is insensitive to ion mass with the exception of the lightest ions like helium. Experimental data analyzed by Sigmund shows that below a keV, there is not a lot of difference between argon, krypton, and xenon sputtering yields of polycrystalline metals such as silver and copper. At high energies of 50 keV or so, xenon has a factor of two greater sputtering yield (atoms/ion) than argon. Rosenberg and Wehner investigate helium, krypton, and xenon sputtering of a wide variety of target materials at 100, 200, 300, and 600 eV ion energies. The yields for krypton and xenon are similar. This research suggests that using argon, or krypton, in place of xenon should not result in differences in sputtering yield at the energies important to HET physics and erosion. At most, there should be a factor of two difference for extremely high energies.

V. Conclusion

A sputtering experiment, designed to test the dependence of plasma erosion on the presence of mechanical stress in materials, is conducted. The experiment investigates fused silica and M26 borosil. Detailed statistics from surface profilometry and microscope images were collected from each sample before and after exposure to plasma. Samples were exposed to an argon plasma for 12 hrs. Compressive stresses in a range from 6 to 25 MPa were applied. Stresses of up to 24.99 ± 1.10 MPa for fused silica, and 24.1 ± 3.4 MPa for M26 are applied to the experiment samples while unstressed control samples are also exposed. Contact profilometry conducted before and after each exposure provide detailed Fourier statistics of the initial and final surfaces of each sample. The surface statistics

reveal that, for the stress ranges tested in this experiment, no difference is discernible between the evolution of the stressed samples and the control samples. For loads of up to 25 MPa, for fused silica and M26, no evidence for the dependence of plasma erosion on mechanical stress is found. The plasma erosion of fused silica and M26 appears to be insensitive to mechanical stress, for these stress levels.

While evidence for an effect dependent on mechanical stress has not been found, explanations are found for the surfaces that are observed to develop for each material. Models that successfully reproduce the features that develop on each material are given. For the amorphous fused silica, the final surface structure that develops is governed by the presence or absence of initial surface structure. In the absence of initial surface structure, flat surfaces remain flat. Where surface roughness is present, a cell-pattern composed of parabolic cells bounded by sharp-edged cusps develops. This pattern can be explained to be the result of the angle dependence of the sputtering yield of fused silica. A 1D model that propagates a surface profile using only an angle-dependent model for the yield of fused silica can reproduce the cell pattern and observed surface statistics. The surfaces that develop on the M26 material are found to be insensitive to an initial surface RMS roughness of $1.55 \pm 0.10 \mu\text{m}$. Consistent post-exposure surface statistics develop that are independent of small variations in the initial surface roughness statistics. The M26 surface can be explained to be the result of the complex heterogeneous microstructure present in this composite material. Modeling of the erosion of a heterogeneous material is investigated in detail in Ref 17.

Acknowledgments

This work was funded by a National Defense Scientific and Engineering Graduate (NDSEG) fellowship, and by the Air Force Office of Scientific Research (AFOSR) under grant number FA9550-11-1-0160. The authors would like to thank the American Society for Engineering Education (ASEE) and AFOSR for supporting this research. In addition, the authors would like to thank Dr. Jud Ready and Dr. Brent Wagner of the Georgia Tech Research Institute for the use of their chamber and plasma source. The authors would like to thank Thomas Burton and Professor Gregory B. Thompson of the University of Alabama for their help conducting SEM microscopy of the AFRL/UM P5 channel wall.

References

- ¹Dudeck, F., Doviell, F., Arcis, N., and Zurbach, S., "Plasma Propulsion for Geostationary Satellites and Interplanetary Spacecraft," *Romanian Journal of Physics*, vol. 56, pp 3-14, Jan 2011.
- ²Clauss, C., Day, M., Kim, V., Kondakov, Y., Randolph, T., "Preliminary study of possibility to ensure large enough lifetime of SPT operating under increased powers," in *33rd Joint Propulsion Conference and Exhibit*, Joint Propulsion Conferences, Seattle, WA, 1997.
- ³Mikellides, I., Katz, I., Hofer, R., Goebel, D., "Magnetic shielding of a laboratory Hall thruster I. Theory and validation," *Journal of Applied Physics*, vol. 115, no. 4, p. 043303, 2014.
- ⁴Gamero-Castano, M., Katz, I., "Estimation of Hall Thruster Erosion using HPHall," in *29th International Electric Propulsion Conference*, Electric Propulsion Rocket Society, Princeton University, 31 Oct 2005.
- ⁵Hofer, R., Mikellides, I., Katz, I., Goebel, D., "BPT-4000 Hall thruster discharge chamber erosion model comparison with qualification life test data," in *30th International Electric Propulsion Conference*, Electric Propulsion Rocket Society, Florence Italy, 2007.
- ⁶Mikellides, I., Hofer, R., Katz, I., Goebel, D., "The Effectiveness of Magnetic Shielding in High-Isp Hall Thrusters," in *49th AIAA/ASME/SAE/ASEE Joint Propulsion Conference*, San Jose, CA, 2013.
- ⁷De Grys, K. H., Mathers, A., Welander, B., Khayms, V., "Demonstration of 10,400 Hours of Operation on 4.5 kW Qualification Model Hall Thruster," in *46th AIAA/ASME/SAE/ASEE Joint Propulsion Conference & Exhibit*, Nashville, TN, 2010.
- ⁸Garner, C., Brophy, J., Polk, J., Pless, I., "A 5,730-hr cyclic endurance test of the SPT-100," in *31st Joint Propulsion Conference and Exhibit*, San Diego, CA, 1995.
- ⁹Zurbach, S., Duchemin, O., Vial, V., Marchandise, N., Conru N., and Arcis, N., "Qualification of the PPS-1350 Hall Thruster at 2.5 kW," in *49th AIAA/ASME/SAE/ASEE Joint Propulsion Conference*, San Jose, CA, July 2013.
- ¹⁰Kim, K-S., Hurtado, A., Tan, H., "Evolution of a surface-roughness spectrum caused by stress in nanometer-scale chemical etching," *Physical Review Letters*, vol. 83, no. 19, pp. 3872-3875, 1999.
- ¹¹Schinder, A. M., Rimoli, J. J., Walker, M. L. R., "Investigation of Plasma Material Erosion under Mechanical Stress," *AIAA Journal of Propulsion and Power*, (In Review).

- ¹²Garnier, Y., Viel, J., Roussel, J. F., Pagnon, D., Mange, L., and Touzeau, M. "Investigation of xenon ion sputtering of one ceramic material used in SPT discharge chamber," in *26th International Electric Propulsion Conference*, Electric Propulsion Rocket Society, Kitakyushu, Japan, 1999.
- ¹³Mazouffre, S., Echegut, P., Dudeck, M., " A calibrated infrared imaging study on the steady state thermal behaviour of Hall effect thrusters," *Plasma Sources Science and Technology*, vol. 16, no. 1, p. 13, 2007.
- ¹⁴Sigmund, P. "Theory of Sputtering. I. Sputtering Yield of Amorphous and Polycrystalline Targets." *Physical Review*, vol. 184, no. 2 (August 10, 1969): 383–416.
- ¹⁵Townsend, P., Kelley, J., Hartley, N., " Chapter 6: Sputtering," in *Ion implantation, sputtering, and their applications*, Academic Press, 1976, pp. 111 - 147.
- ¹⁶Yalin, A. P., Rubin, B., Domingue, S. R., Glueckert, Z., Williams, J. D., " Differential Sputter Yields of Boron Nitride, Quartz, and Kapton Due to Low Energy Xe+ Bombardment," AIAA Paper 5314-2007, American Institute of Aeronautics and Astronautics, 2007.
- ¹⁷Schinder, A., Walker, M., and Rimoli, J. "3D Model for Erosion of a Hall Effect Thruster Discharge Channel Wall." *Journal of Propulsion and Power*, vol. 30, no. 5 (2014): 1373–82. doi:10.2514/1.B35098.
- ¹⁸Haas, J. M., "Low-perturbation interrogation of the internal and near-field plasma structure of a Hall thruster using a high-speed probe positioning system," PhD. Dissertation, University of Michigan, 2001.
- ¹⁹Rosenberg, D., and G. K. Wehner. "Sputtering Yields for Low Energy He+, Kr+, and Xe+-Ion Bombardment." *Journal of Applied Physics*, vol. 33, no. 5, pp. 1842–45. 1962.
- ²⁰"COMBAT Boron Nitride Solids: Product Datasheet," St. Gobain Ceramic Materials, [online manufacturers property sheet], 2011, <http://www.bn.saint-gobain.com/combat-bn-solids.aspx> [retrieved 5 Apr 2016].